Electronic Supplementary Information (ESI†)

Ruthenium single atoms implanted on NiS_2–FeS_2 nanosheet heterostructures for efficacious water electrolysis

Ram Babu Ghising[a], Uday Narayan Pan[a], Mani Ram Kandel[a], Purna Prasad Dhakal[a], Saleem Sidra[b], Do Hwan Kim[b], Nam Hoon Kim[a]*, Joong Hee Lee[a,c]*

[a]Department of Nano Convergence Engineering (BK21 four), Jeonbuk National University, Jeonju, Jeonbuk, 54896, Republic of Korea

[b]Division of Science Education, Graduate School, Department of Energy Storage/Conversion Engineering, Jeonbuk National University, Jeonju, Jeonbuk, 54896, Republic of Korea

[c]Carbon Composite Research Center, Jeonbuk National University, Jeonju, Jeonbuk, 54896, Republic of Korea.

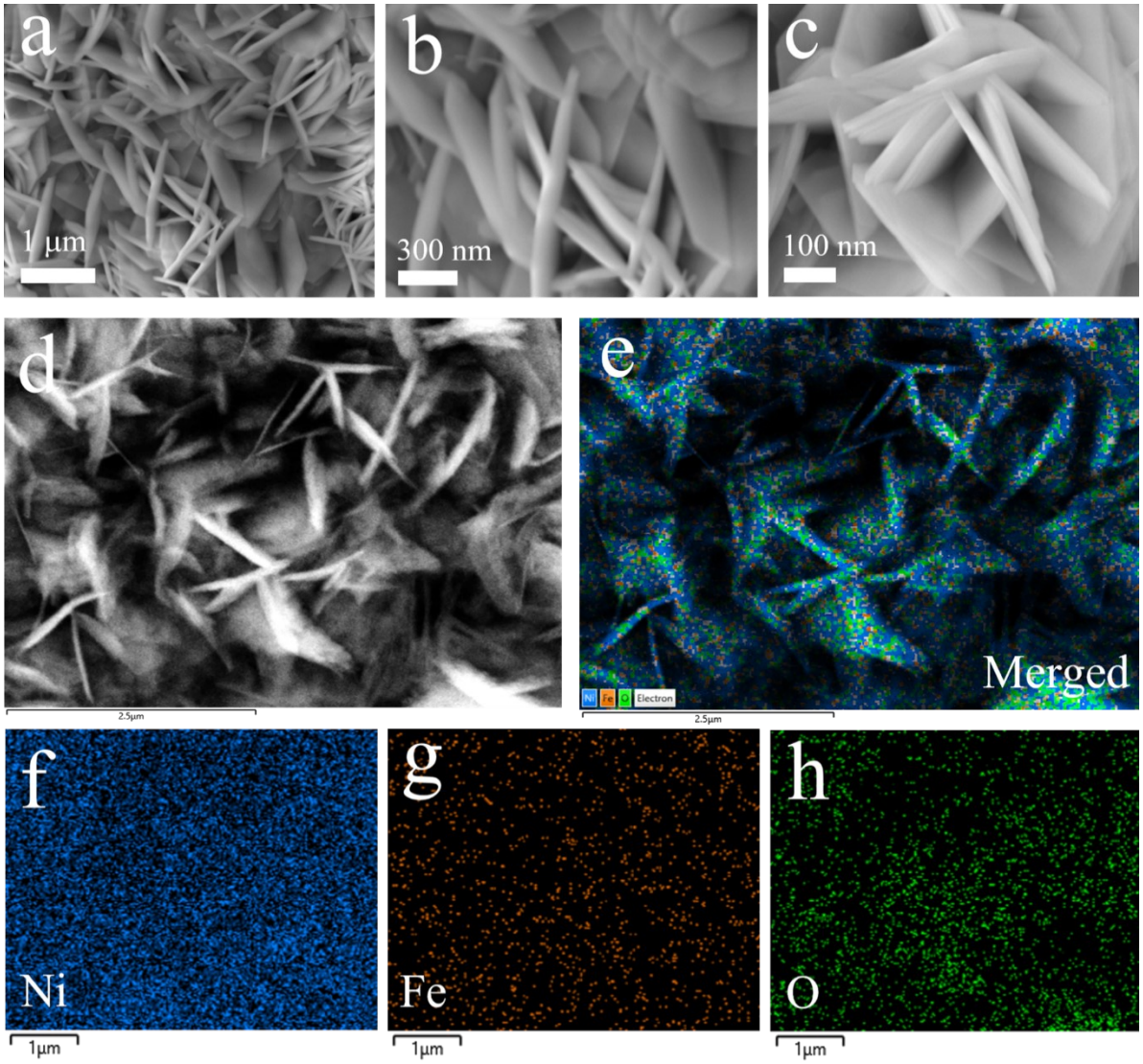

Fig. S1: (**a-c)** FE-SEM images of NiFe-LDH from low to high magnifications. (**d**) FE-SEM electronic image, (**e**) EDS layered image, and (**f-h**) SEM-EDS color mappings of individual elements Ni, Fe, and O of NiFe-LDH.

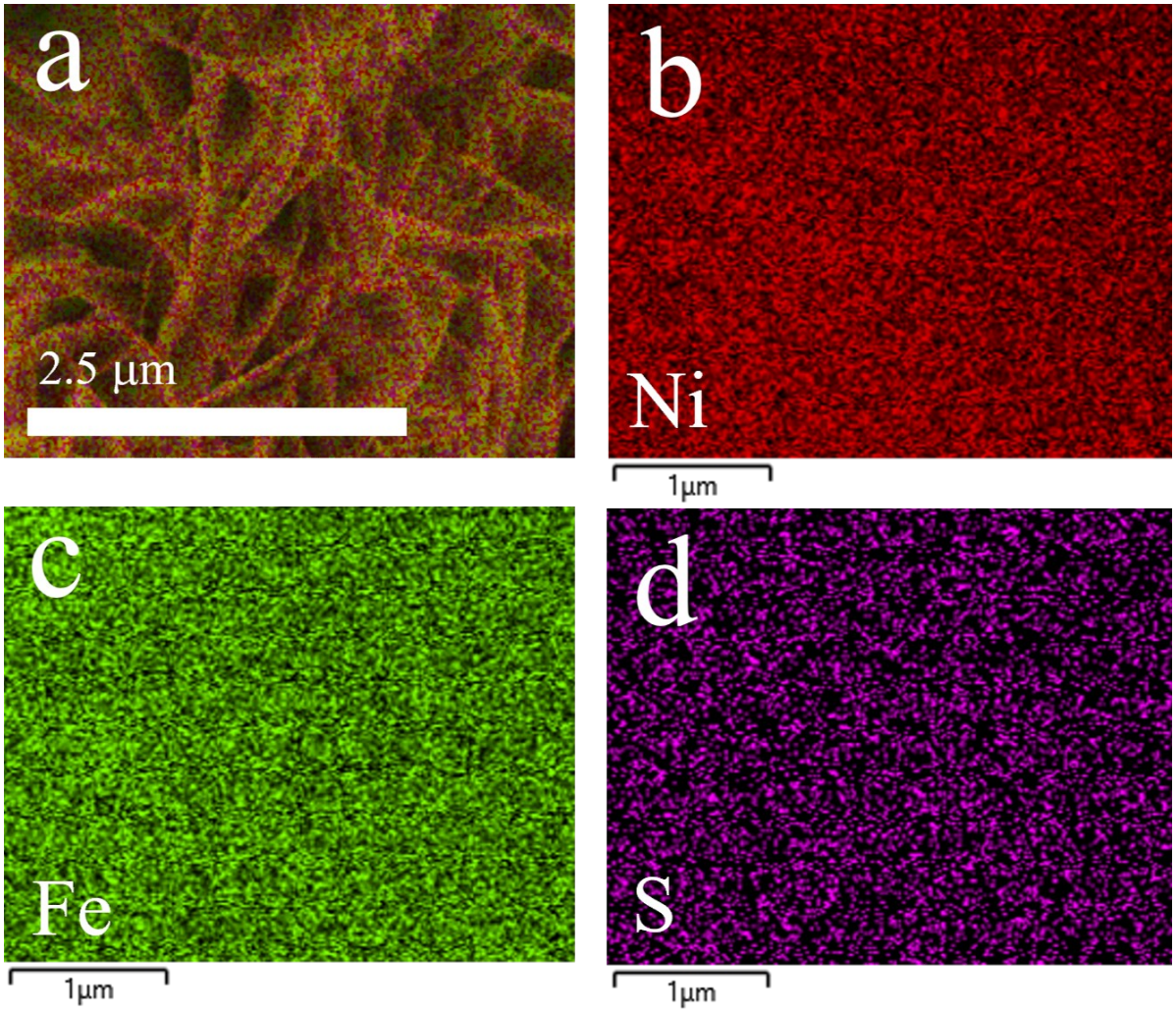

Fig. S2: (**a**) Merged color mappings, and (**b-d**) FE-SEM EDS color mappings of individual elements like Ni, Fe and S of NiS_2-FeS_2.

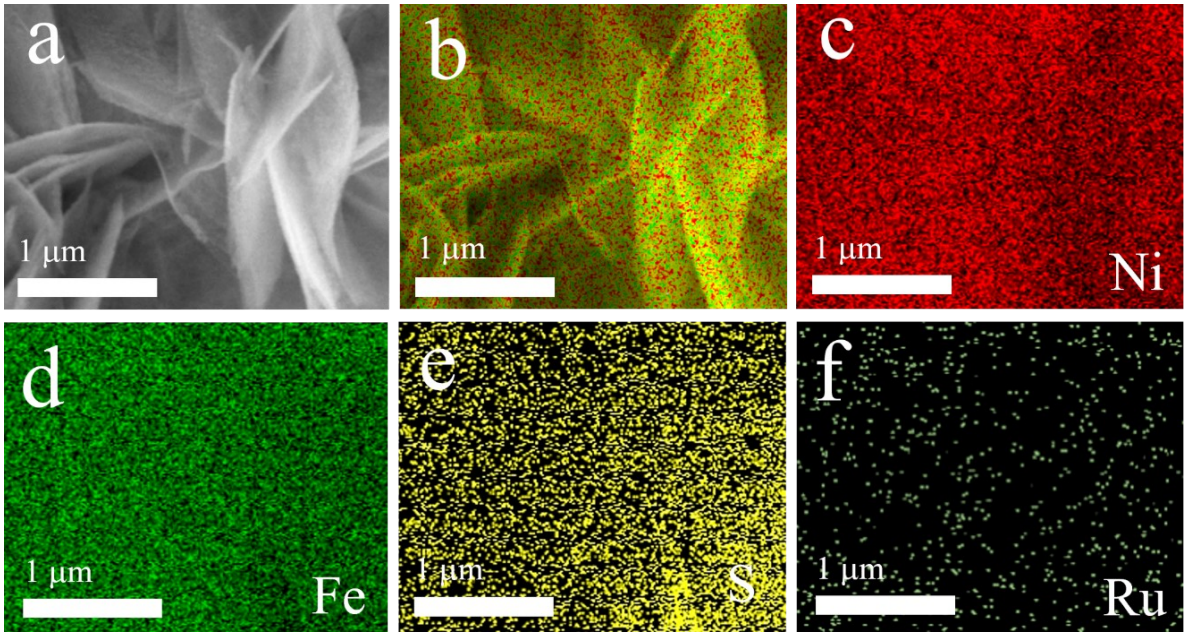

Fig. S3: FE-SEM and EDS images of Ru_{SA}-NiS_2-FeS_2: (**a**) Electronic image, (**b**) EDS layered image, (**c-f**) Individual color mappings of Ni, Fe, S and Ru of Ru_{SA}-NiS_2-FeS_2.

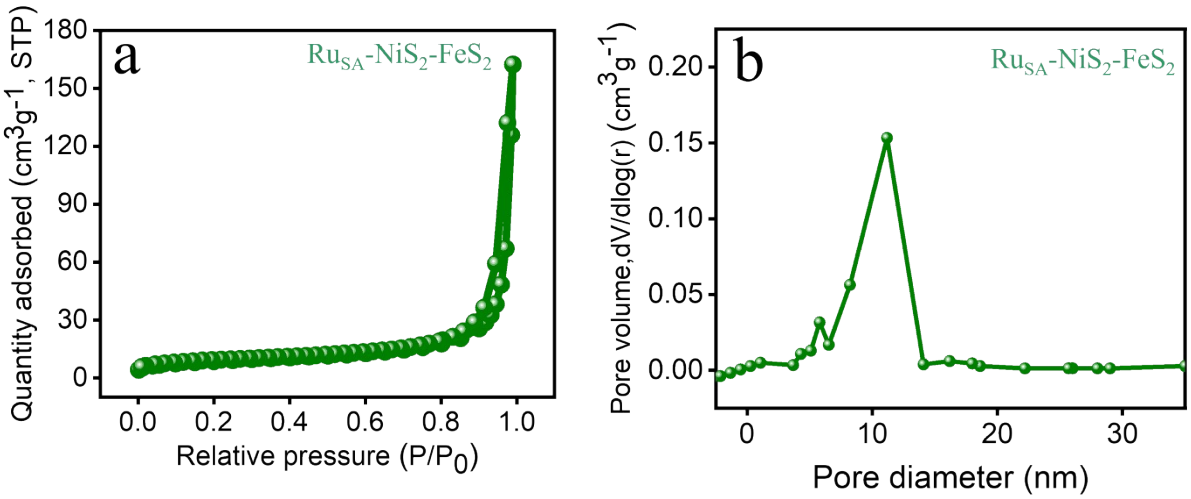

Fig. S4: Specific surface area and pore size distribution of Ru_{SA}-NiS_2-FeS_2.

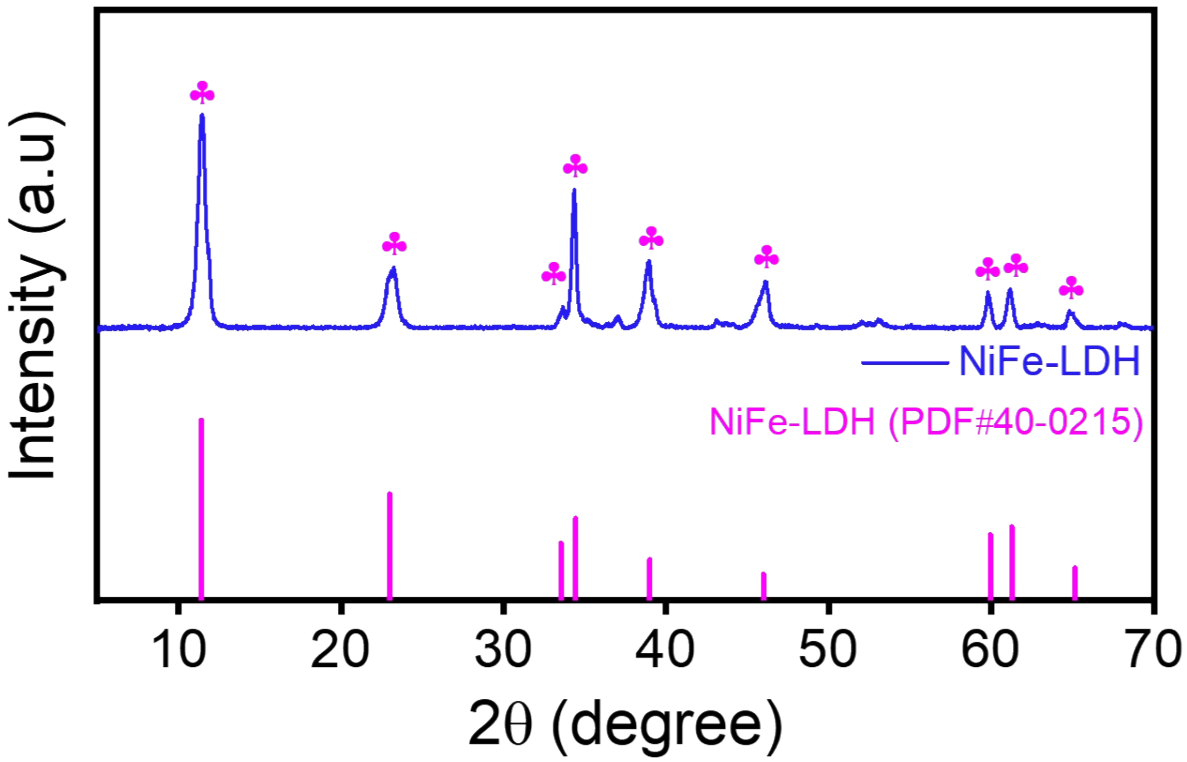

Fig. S5: PXRD analysis of NiFe-LDH.

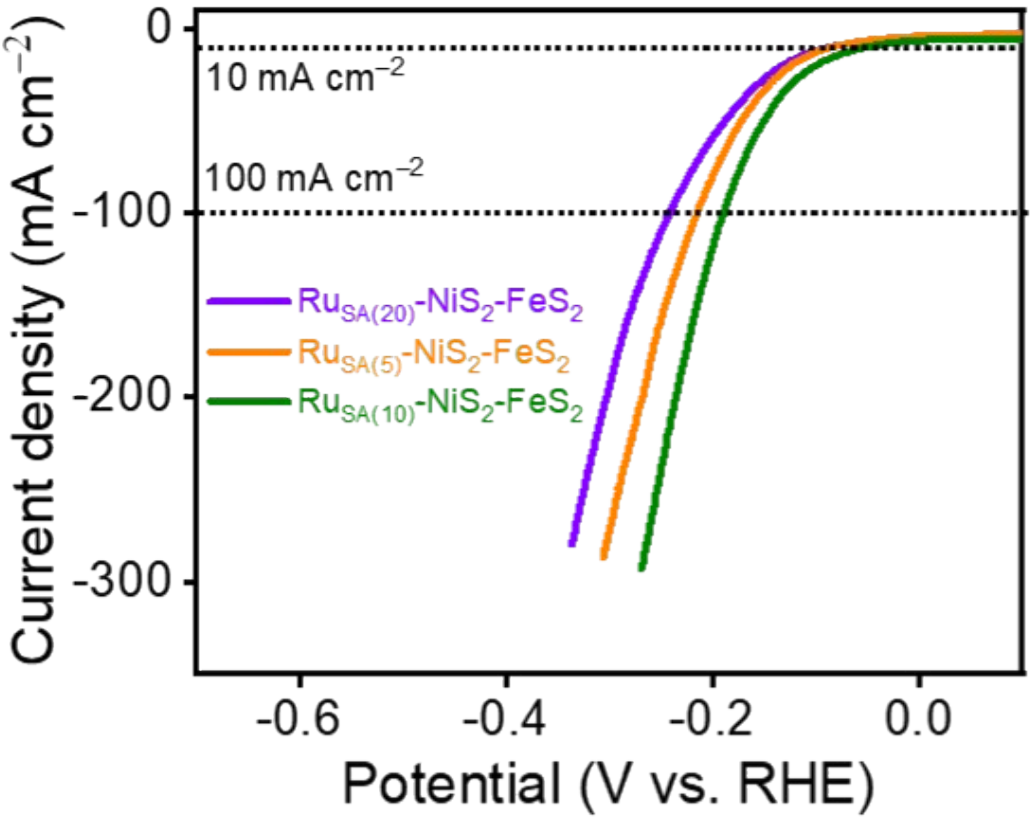

Fig. S6: LSV curves of electrocatalytic materials towards HER performance at varying contents of Ru.

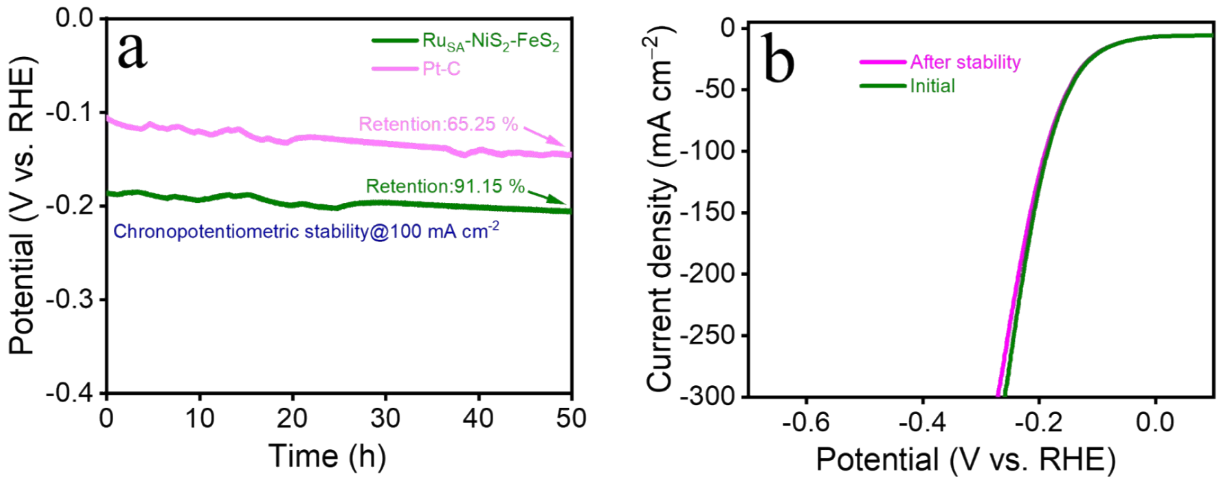

Fig. S7: (**a**) Long-term stability analysis of Ru_{SA}-NiS_2-FeS_2 and commercial Pt-C using chronopotentiometry (CP) technique. (**b**) LSV polarization curves of Ru_{SA}-NiS_2-FeS_2 before and after long term HER stability test.

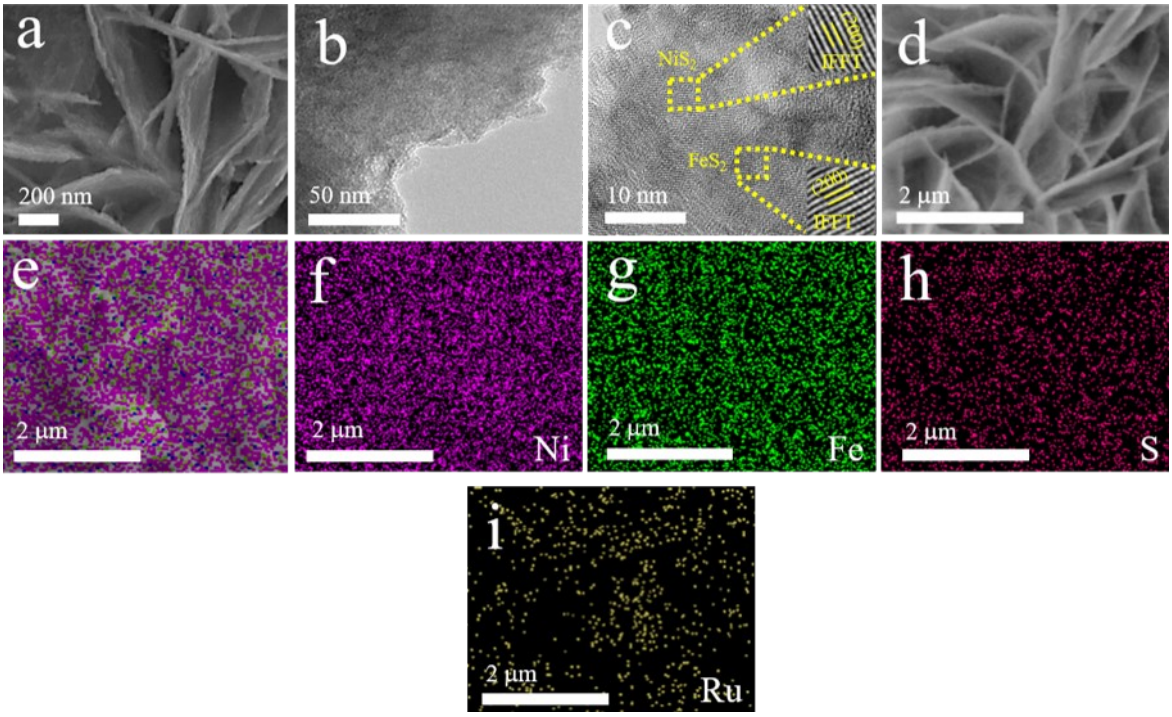

Fig. S8: After HER stability: (**a**) FE-SEM image, (**b**) TEM image, (**c**) HR-TEM image, (**d**) Electronic image of Ru_{SA}-NiS_2-FeS_2, (**e**) EDS layered image of Ru_{SA}-NiS_2-FeS_2 (**f-h**) Elemental color mappings of Ni, Fe, S, and Ru of Ru_{SA}-NiS_2-FeS_2.

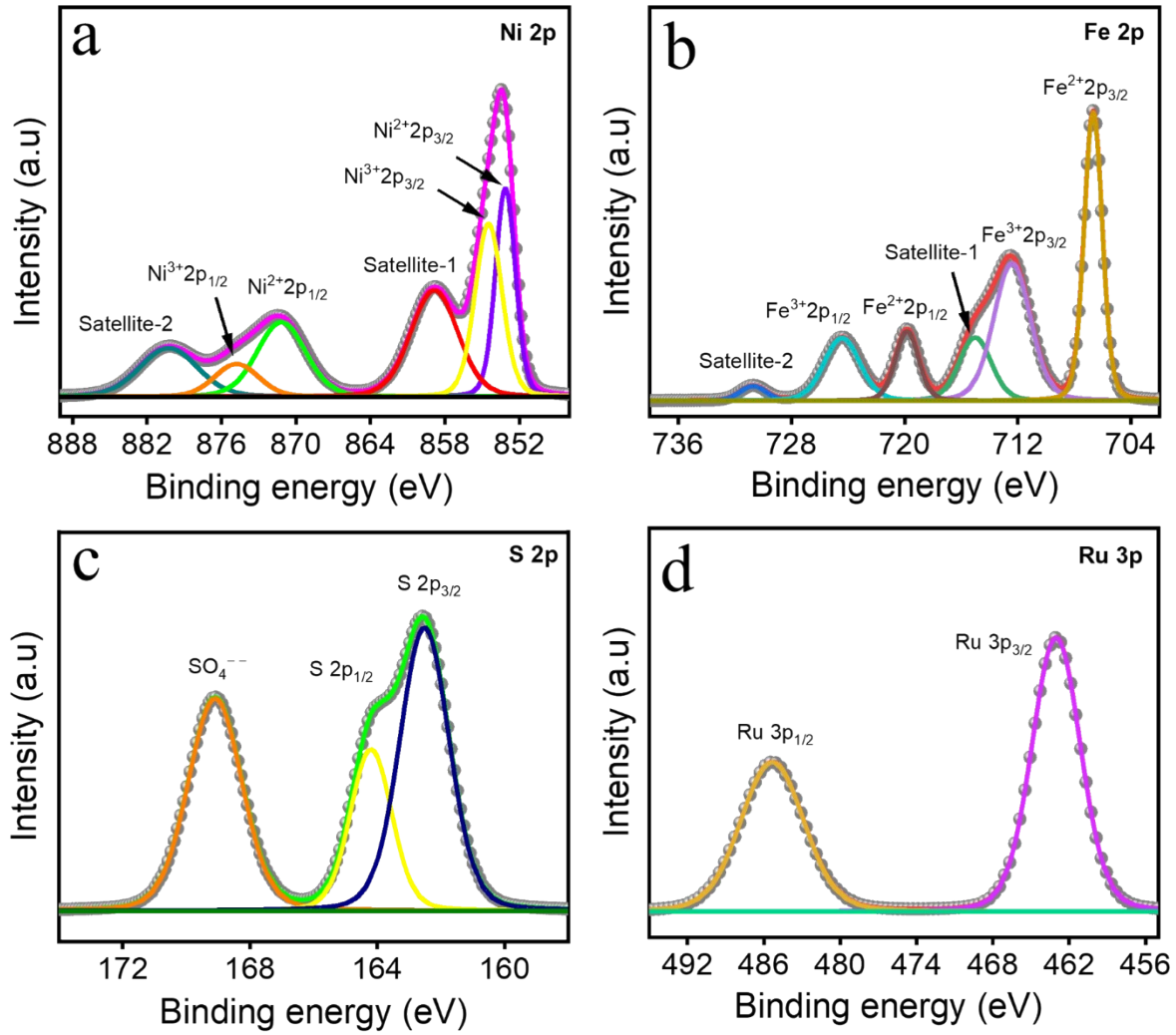

Fig. S9: (a) High-resolution XPS (HR-XPS) spectra of (**a**) Ni 2p, (**b**) Fe 2p, (**c**) S 2p, and (**d**) Ru 3p, of Ru_{SA}-NiS_2-FeS_2 after HER stability.

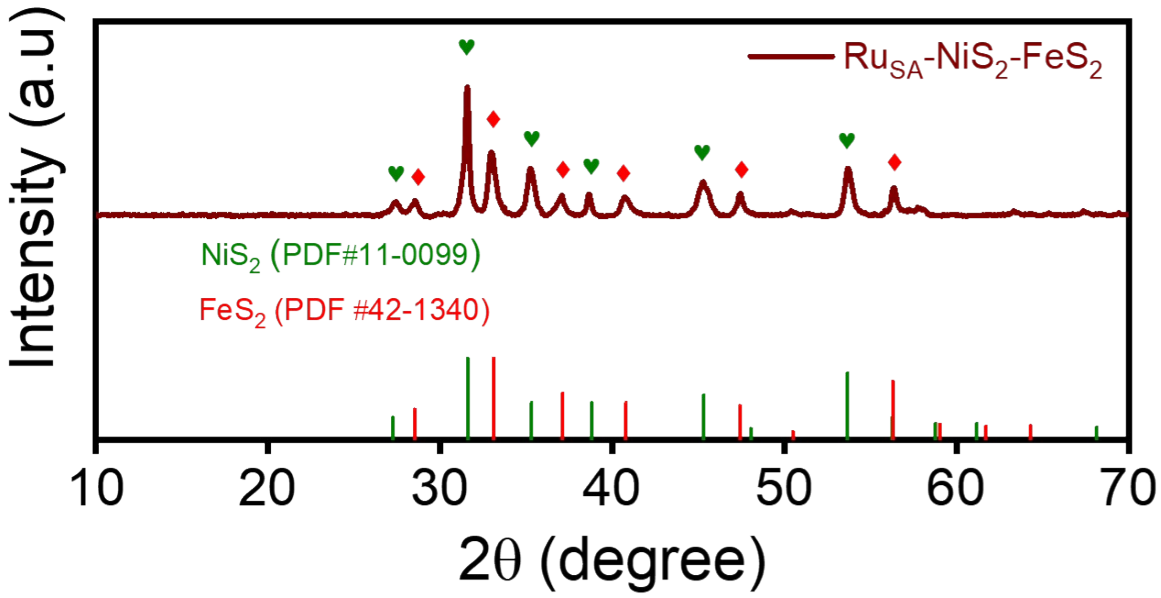

Fig. S10: PXRD patterns of Ru_{SA}-NiS_2-FeS_2 after HER stability test.

Table S1: Comparative HER catalytic activity of Ru_{SA}-NiS_2-FeS_2 with the recently reported electrocatalysts.

Electrocatalysts	Overpotential (mV) @10 mA cm^{-2}	References
Ru_{SA}-NiS_2-FeS_2	**57**	**This work**
NiS_2/VS-3:1	74	[1]
NiFe-LDH/MoS_2-Ni_3S_2/NF	79	[2]
MnS_xSe_{1-x}@N,F-CQDs	87	[3]
$NiFeCoS_x$@$FeNi_3$	88	[4]
FeS_2-MoS_2@CoS_2-MOF	92	[5]
Mn-NiS_x/NiO/Ni_3N@NF	93	[6]
CoNi-SP/NPC	105	[7]
SnO_2@MoS_2/NF	127	[8]
Ni_2FeS@NSC	271	[9]
CNTs@Ir-$CoNi_2S_4$	271.3	[10]

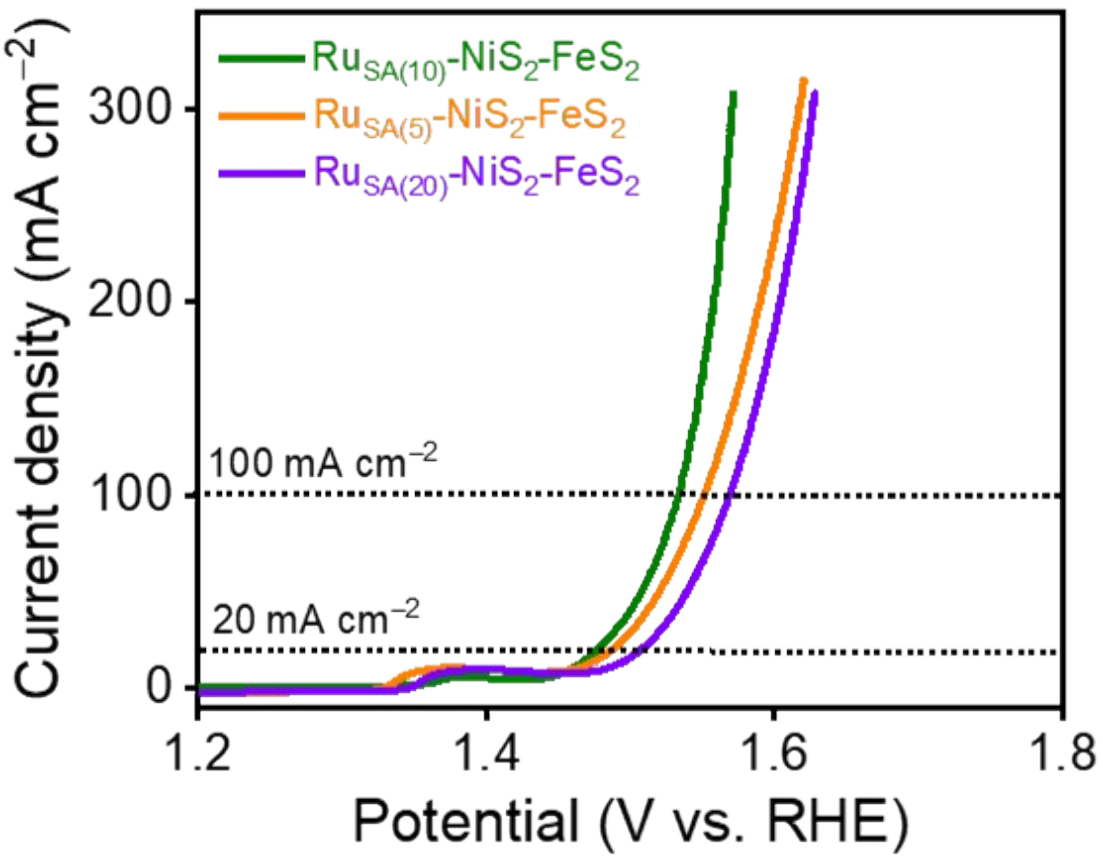

Fig. S11: LSV curves of electrocatalytic materials towards OER performance at varying contents of Ru.

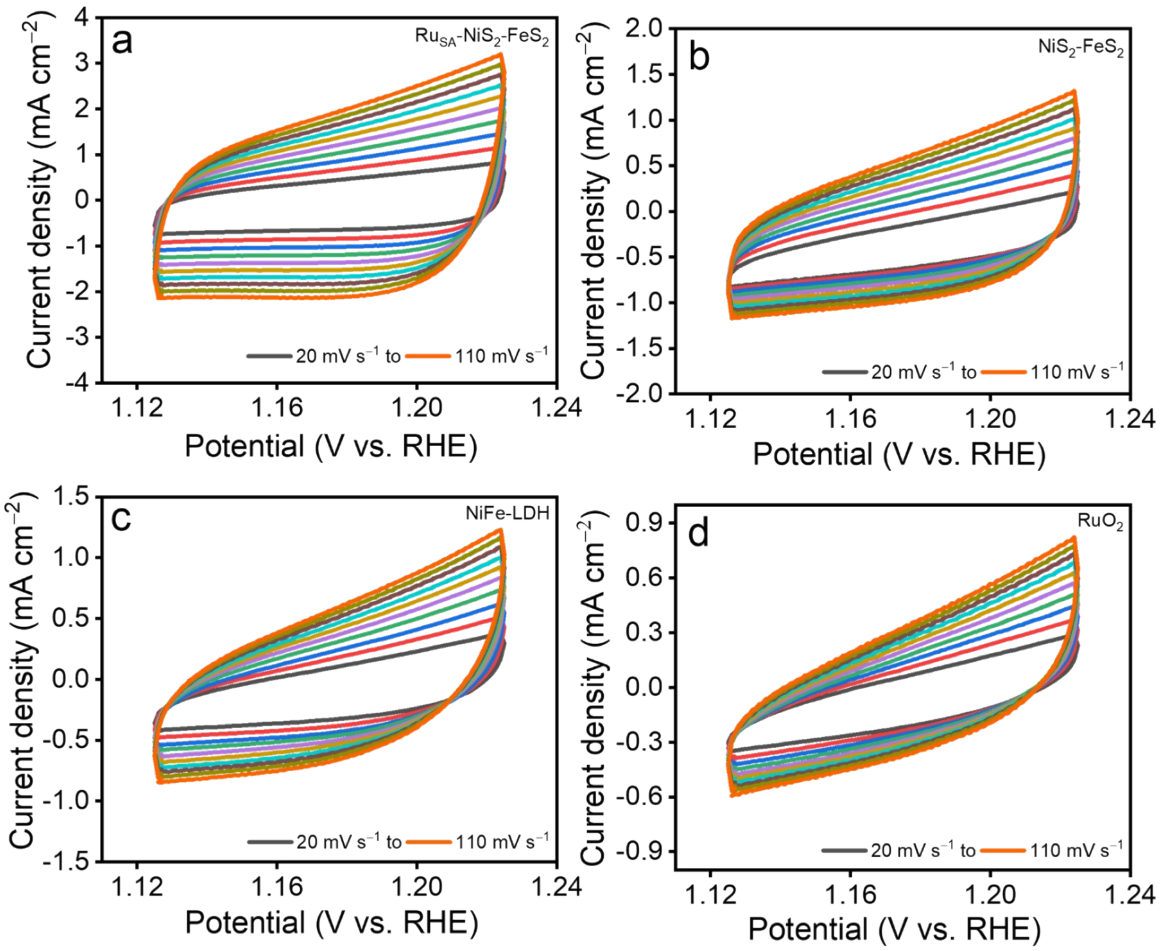

Fig. S12: Cyclic voltammograms (CV) of different electrolytic materials with scan rates ranging from 20 to 110 mV s^{-1}.

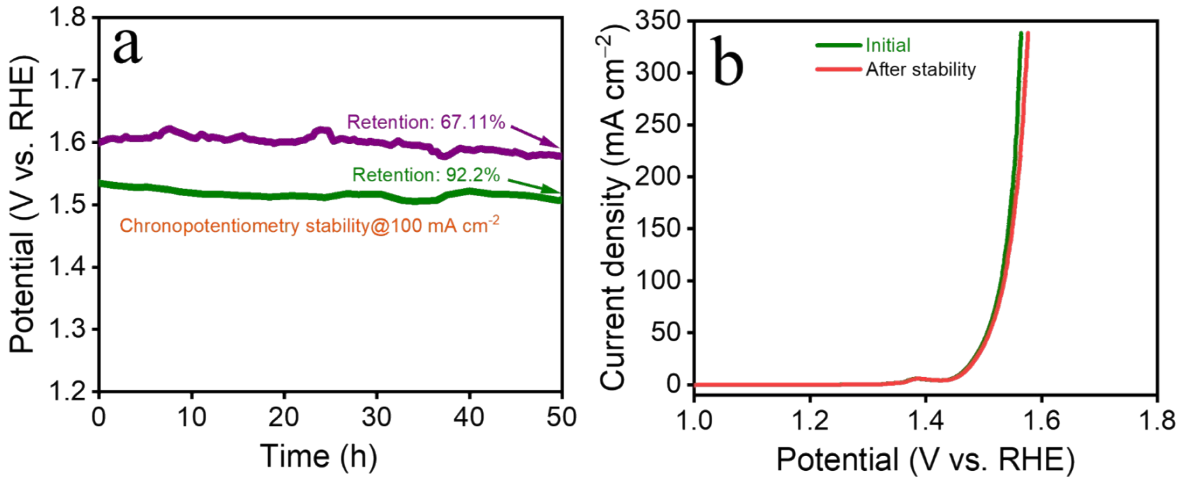

Fig. S13: (**a**) Long-term stability analysis of Ru_{SA}-NiS_2-FeS_2 and commercial RuO_2 using chronopotentiometry (CP) technique. (**b**) LSV polarization curves of Ru_{SA}-NiS_2-FeS_2 before and after long term OER stability test.

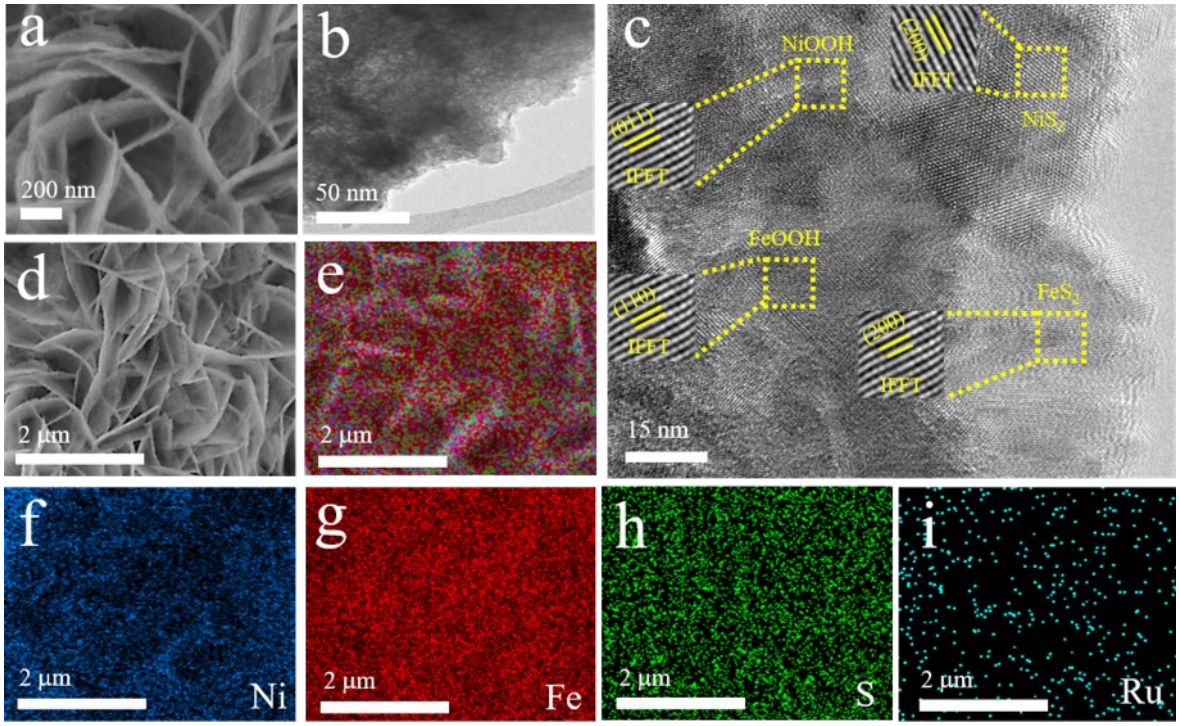

Fig. S14: After OER stability: (**a**) FE-SEM image, (**b**) TEM image, (**c**) HR-TEM image of Ru_{SA}-NiS_2-FeS_2 with formation of metal oxyhydroxides, (d) Electronic image of Ru_{SA}-NiS_2-FeS_2, (**e**) EDS layered image of Ru_{SA}-NiS_2-FeS_2 (**f-i**) Elemental color mappings of Ni, Fe, S, and Ru of Ru_{SA}-NiS_2-FeS_2.

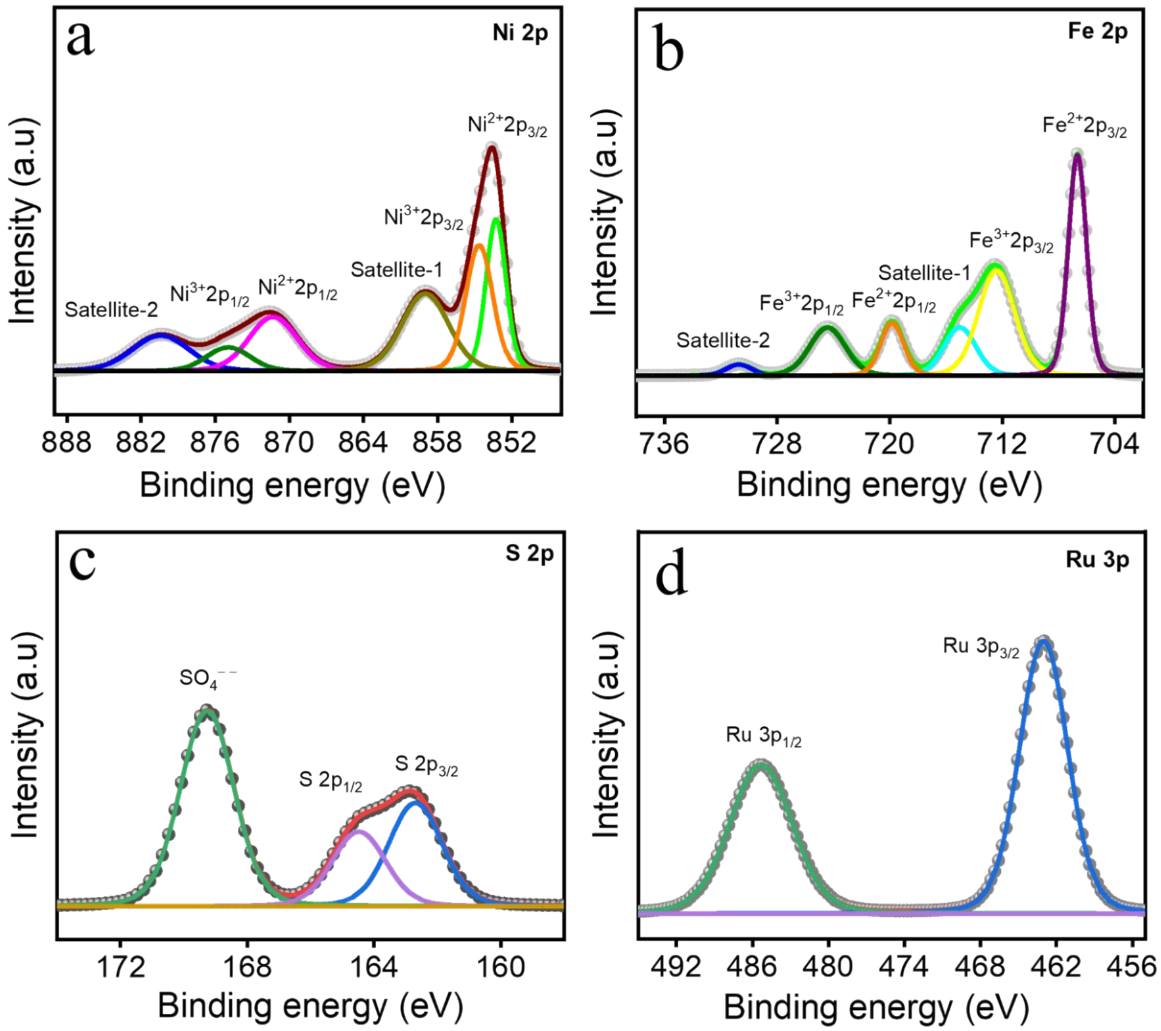

Fig. S15 : (a) High-resolution XPS (HR-XPS) spectra of (**a**) Ni 2p, (**b**) Fe 2p, (**c**) S 2p, and (**d**) Ru 3p, of Ru_{SA}-NiS_2-FeS_2 after OER stability.

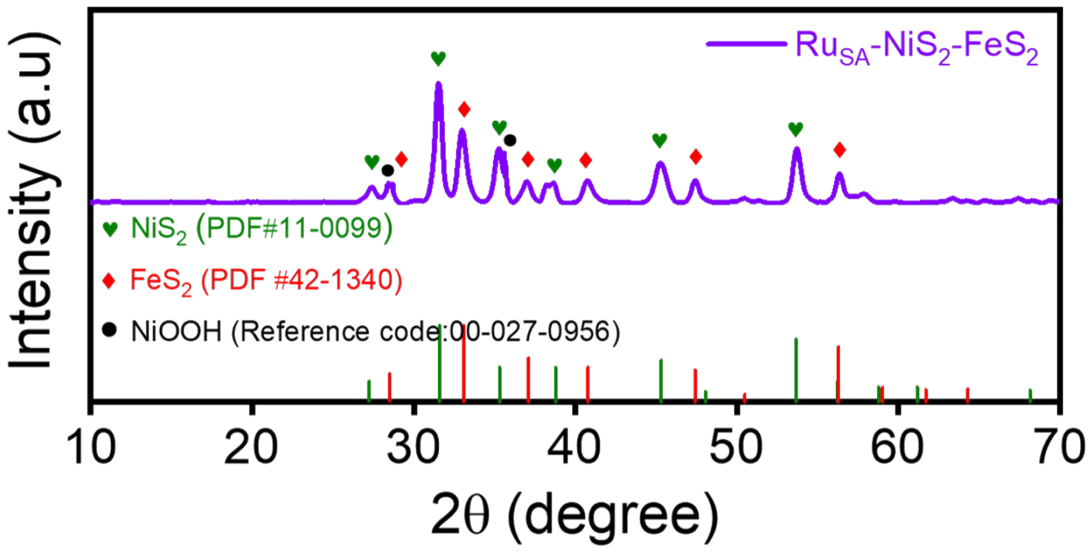

Fig. S16: PXRD patterns of Ru_{SA}-NiS_2-FeS_2 after OER stability test.

Density functional Theory (DFT) calculation

To explore the crystal structure of the ruthenium single atoms incorporated NiS_2-FeS_2 heterostructures, we employed the Vienna Ab initio Simulation Package (VASP) based on the Density Functional Theory (DFT) method, in different applications including hydrogen evolution reaction (HER) and oxygen evolution reaction (OER). Initially, the materials were optimized to get stable structures.[11] The Perdew–Burke–Ernzerhof (PBE) exchange-correlation functional in the form of Generalized Gradient Approximation (GGA) was applied in this theoretical investigation.[12] To mitigate interactions between adjacent layers, 15 Å vacuum slabs were implemented. A plane wave basis set with an energy cut-off of 420 eV was used, and the projector augmented wave (PAW) method described electron-ion interactions. Grimme's DFT-D3 functional, based on a semi-empirical GGA-type theory, was employed to correct dispersion forces.[13] Structural relaxation continued until the Hellman-Feynman forces were below 0.02 eV/Å.

The cubic unit cell of NiS_2 (PDF # 11-0099) in the space group Pa-3(205) was optimized using a Brillouin zone sampling of 8 x 8 x 8 Monkhorst-Pack K-Points, with lattice constants a=b=c= 5.670 Å and angles α=β=γ=90̊. Correspondingly, the cubic unit cell of FeS_2 (PDF# 42-1340) in the space group Pa-3(205) was optimized under the same conditions. Afterward, a surface was constructed using the unit cells of NiS_2 and FeS_2 in the (200) plane, with a 15 Å vacuum applied in the z-direction.

NiS_2 and FeS_2 were then combined into a heterostructure, and Ru single atoms were doped according to experimental data. Following the formation of the Ru_{SA}-NiS_2-FeS_2 heterostructure, optimization was carried out with 5 x 5 x 1 K-points. During the structure optimization, half layers of Ru_{SA}-NiS_2-FeS_2 were fixed, and the remaining half layers were relaxed.

H-adsorption energy (ΔH*) and Gibbs free energy change (ΔG_{H^*}) in HER:

The hydrogen adsorption energy (ΔH*) is a critical parameter for assessing the material's HER capability. And, the calculation is based on the formula.[14]

$$\Delta H^* = E_{H^*/slab} - E_{slab} - (E_{H2})_{/2} \quad (1)$$

Where, $E_{H^*/slab}$, E_{slab}, and $(E_{H2})_{/2}$ represent the energy of the material after H* adsorption on the surface, the VASP energy or clean surface energy, and the energy of the isolated hydrogen molecule, respectively. Materials with energetically less favourable conditions exhibit higher catalytic stability and contains more stable hydrogen adsorption sites.[15]

The Gibbs free energy change for H* adsorption was calculated using the formula proposed by Norskov et al.[16]

$$\Delta G_{H^*} = E_{H^*} - E_{surf} - (E_{H2})/2 + \Delta E_{ZPE} - T\Delta S \quad (2)$$

where E_{H^*}, E_{surf}, E_{H2}, ΔE_{ZPE}, and ΔS represent the total energies of the slab with the H-adsorbed surface, tl

Gibbs free energy changes in OER:

In our research, we have also computed the four steps of the OER in alkaline conditions on various active sites. The electron mechanism for the four steps in OER is outlined below.[16]

$$OH^- + * \rightarrow OH^* + e^- \quad \Delta G_1 \quad (3)$$

$$OH^- + OH^* \rightarrow O^* + H_2O + e^- \quad \Delta G_2 \quad (4)$$

$$O^* + OH^- \rightarrow OOH^* + e^- \quad \Delta G_3 \quad (5)$$

$$OOH^* + OH^- \rightarrow O_2 + * + H_2O + e^- \quad \Delta G_4 \quad (6)$$

In these equations (3-6), OH, O, and OOH represent the adsorption sites of the oxygen evolution reaction on the surface of the electrocatalyst at various active sites. The Gibbs free

energy is calculated using these adsorption sites. Subsequently, we determined the theoretical overpotential (η) of the catalyst material using the formula provided below.[17]

$$\eta OER = \frac{max\{\Delta G_1, \Delta G_2, \Delta G_3, \Delta G_4\}}{e} - 1.23\ (V) \tag{7}$$

The symbols ΔG_1, ΔG_2, ΔG_3, and ΔG_4 represent the Gibbs free energies changes in OER steps.[18]

Table S2: Comparative OER catalytic activity of Ru_{SA}-NiS_2-FeS_2 with the recently reported electrocatalysts.

Electrocatalysts	Overpotential (mV@mA cm^{-2})	References
Ru_{SA}-NiS_2-FeS_2	**242@20**	**This work**
NiS_2/VS-3:1	235@10	[1]
VTe_2@ZnFeTe/NF	240@20	[19]
Fe MOF-Ni_3S_2/NF	243@100	[20]
Fe-NiS_2/NCNT	247@100	[21]
$NiFe_2O_4$@(Ni,Fe)S/P	261@10	[22]
CoVRu LDH	263@25	[23]
MoP_xS_y@$NiFeP_xS_y$@NPS-C	274@10	[24]
NiCoS/NF	287@10	[25]
SnO_2@MoS_2/NF	290@50	[8]
CoNi-SP/NPC	313@100	[7]

Table S3. ΔH*-adsorption energy and Gibbs free energy change of Ru_{SA}-NiS_2-FeS_2 at Ru, Ni, Fe, and S active-sites, respectively.

Catalyst	Adsorption sites	ΔH*-Adsorption energy (E_{ads}, eV)	Gibbs Free Energy (ΔG_{H*}, eV)
*Ru_{SA}-NiS_2-FeS_2	Ru	-0.065	-0.101
Ru_{SA}-*NiS_2-FeS_2	Ni	-0.108	-0.170
Ru_{SA}-NiS_2-*FeS_2	Fe	-0.259	-0.182
Ru_{SA}-NiS_2-Fe*S_2	S	-0.277	-0.195

Table S4. The theoretical Gibbs free energy change at different steps for Ru_{SA}-NiS_2-FeS_2 during OER mechanism along with theoretical OER overpotential values at Ru, Ni, Fe, and S active-sites, respectively.

Catalyst	Adsorption sites	Gibbs free energy change ΔG_T (eV)				OER Overpotential (η , V)
		ΔG1	ΔG2	ΔG3	ΔG4	
Ru_{SA}-NiS_2-FeS_2	Ru	0.701	0.846	1.659	1.715	0.48
	Ni	1.499	0.115	1.658	1.649	0.43
	Fe	0.753	-0.019	2.112	2.074	0.88
	S	1.051	0.244	1.856	1.769	0.63

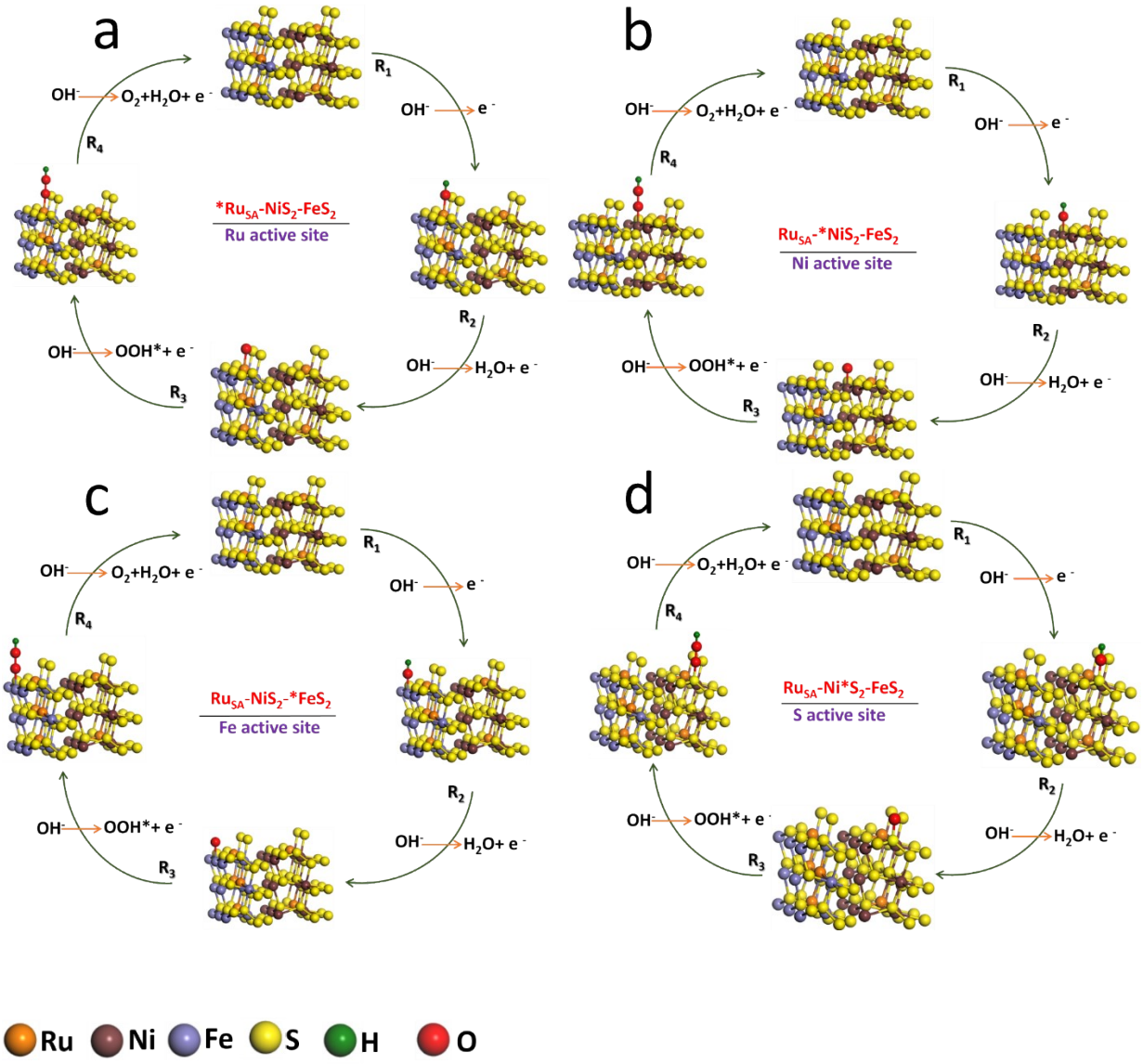

Fig. S17. The OER mechanism pathways for Ru_{SA}-NiS_2-FeS_2 at Ru, Ni, Fe, and S active-sites respectively.

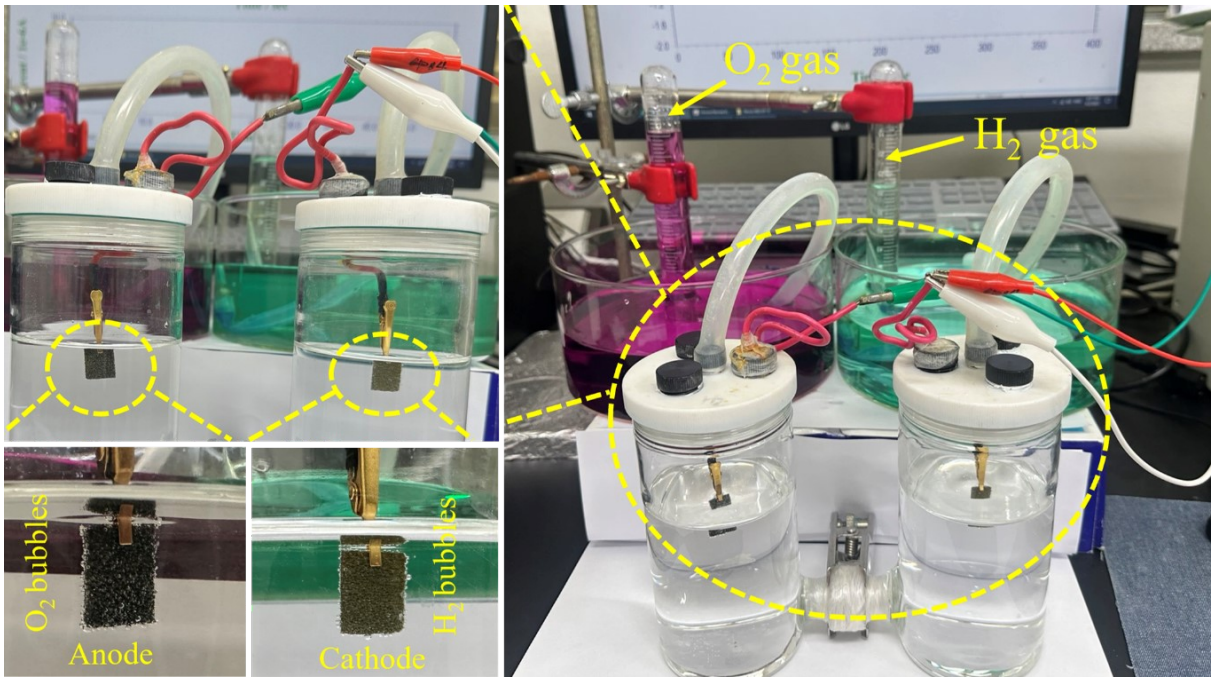

Fig. S18: Faradaic efficiency (FE) measurement using the laboratory-made two-electrode set up of alkaline electrolyzer assembled with Ru_{SA}-NiS_2-FeS_2, working as both anode and cathode during water splitting.

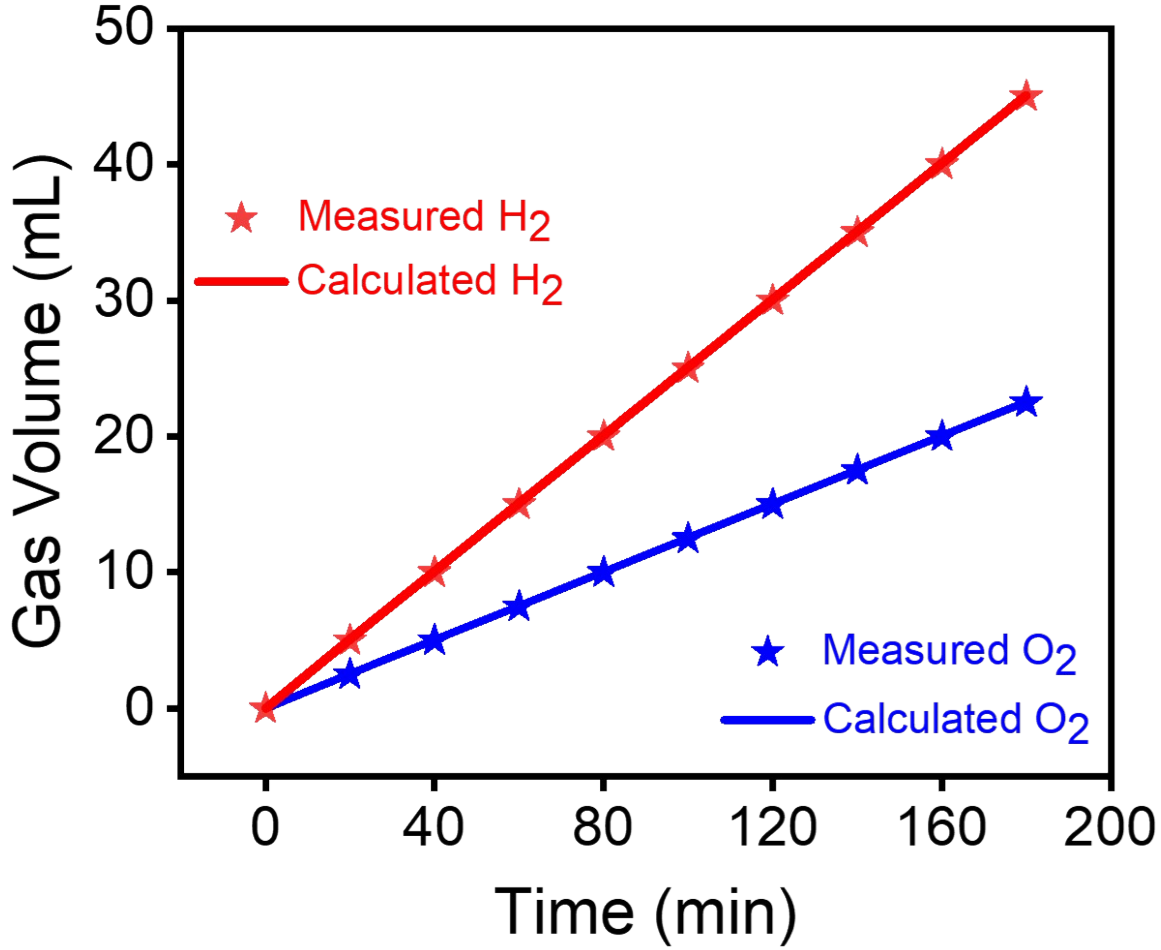

Fig. S19: Plot showing the calculated and experimental H_2 and O_2 volume ratio during Faradaic efficiency (FE) measurement.

Table S5: Comparative cell voltage of Ru_{SA}-NiS_2-FeS_2 device with the recently reported bifunctional electrocatalysts.

Bifunctional electrocatalysts	Cell voltage (V@10 mA cm^{-2})	References
Ru_{SA}-NiS_2-FeS_2	**1.47**	**This work**
NiFe-LDH/MoS_2-Ni_3S_2/NF	1.50	[2]
FeS_2-MoS_2@CoS_2-MOF	1.51	[5]
CoVRu LDH	1.52	[23]
MnS_xSe_{1-x}@N,F-CQDs	1.55	[3]
$FeNi_2S_4$/CoFe	1.56	[26]
SnO_2@MoS_2/NF	1.57	[8]
VTe_2@ZnFeTe/NF	1.58	[19]
CNTs@Ir-$CoNi_2S_4$ NSs	1.60	[10]
NSQDs@NiFe-TPA	1.66	[27]
NiFeS@NSCs	1.77	[9]

References

1 K. Wu, H. Li, C. Lyu, J. Cheng, Y. Yang, X. Zhu, W. M. Lau and J. Zheng, *J. Alloys Compd.*, 2023, **945**, 169290.

2 S. Wang, X. Ning, Y. Cao, R. Chen, Z. Lu, J. Hu, J. Xie and A. Hao, *Inorg. Chem.*, 2023, **62**, 6428–6438.

3 B. Sun, G. Dong, J. Ye, D. feng Chai, X. Yang, S. Fu, M. Zhao, W. Zhang and J. Li, *Chem. Eng. J.*, 2023, **459**, 141610.

4 J. Shen, Q. Li, W. Zhang, Z. Cai, L. Cui, X. Liu, J. Liu, J. Liu and X. Liu, *J. Mater. Chem. A*, 2022, **10**, 5442–5451.

5 K. Chhetri, A. Muthurasu, B. Dahal, T. Kim, T. Mukhiya, S.-H. Chae, T. H. Ko, Y. C. Choi and H. Y. Kim, *Mater. Today Nano*, 2022, **17**, 100146.

6 P. Yi, Y. Song, C. Li, R. Liu and J. Sun, *Appl. Surf. Sci.*, 2023, **619**, 156789.

7 S. Chen, W. Liang, X. Wang, Y. Zhao, S. Wang, Z. Li, S. Wang, L. Hou, Y. Jiang and F. Gao, *J. Alloys Compd.*, 2023, **931**, 167575.

8 W. He, L. Wang, H. Zhang, S. Gao, W. Yu, D. Yin and X. Dong, *J. Alloys Compd.*, 2023, **938**, 168678.

9 J. Chang, S. Zang, F. Song, W. Wang, D. Wu, F. Xu, K. Jiang and Z. Gao, *Appl. Catal. A Gen.*, 2022, **630**, 118459.

10 X. Zhu, D. C. Nguyen, S. Prabhakaran, D. H. Kim, N. H. Kim and J. H. Lee, *Mater. Today Nano*, 2023, **21**, 100296.

11 G. Kresse and J. Furthmüller, *Comput. Mater. Sci.*, 1996, **6**, 15–50.

12 D. Joubert, *Phys. Rev. B - Condens. Matter Mater. Phys.*, 1999, **59**, 1758–1775.

13 D. Bogdanovski, P. J. Pöllmann and J. M. Schneider, *Nanoscale*, 2022, **14**, 12866–12874.

14 J. Balamurugan, T. T. Nguyen, D. H. Kim, N. H. Kim and J. H. Lee, *Appl. Catal. B Environ.*, 2021, **286**, 119909.

15 J. K. Nørskov, T. Bligaard, A. Logadottir, J. R. Kitchin, J. G. Chen, S. Pandelov and U. Stimming, *J. Electrochem. Soc.*, 2005, **152**, J23.

16 J. K. Nørskov, J. Rossmeisl, A. Logadottir, L. Lindqvist, J. R. Kitchin, T. Bligaard and H. Jónsson, *J. Phys. Chem. B*, 2004, **108**, 17886–17892.

17 S. Prabhakaran and D. H. Kim, *Appl. Surf. Sci.*, 2023, **614**, 156255.

18 S. Ramakrishnan, D. B. Velusamy, S. Sengodan, G. Nagaraju, D. H. Kim, A. R. Kim and D. J. Yoo, *Appl. Catal. B Environ.*, 2022, **300**, 120752.

19 J. Gautam, D. Chanda, M. M. Meshesha, S. G. Jang and B. L. Yang, *Chem. Eng. J.*, 2023, **467**, 143535.

20 X.-Y. Wang, M. Zhu, Q.-N. Bian, B.-S. Guo, W.-Q. Kong, C.-B. Wang and Y.-Y. Feng, *ACS Appl. Nano Mater.*, , DOI:10.1021/acsanm.2c05104.

21 X. Liu, X. Zhao, S. Cao, M. Xu, Y. Wang, W. Xue and J. Li, *Appl. Catal. B Environ.*, 2023, **331**, 122715.

22 Y. L. Wang, T. H. Yang, S. Yue, H. B. Zheng, X. P. Liu, P. Z. Gao, H. Qin and H. N. Xiao, *ACS Appl. Mater. Interfaces*, 2023, **15**, 11631–11641.

23 K. Zeng, M. Tian, X. Chen, J. Zhang, M. H. Rummeli, P. Strasser, J. Sun and R. Yang, *Chem. Eng. J.*, 2023, **452**, 139151.

24 X. Zeng, H. Zhang, R. Yu, G. D. Stucky and J. Qiu, , DOI:10.1039/d3ta01993d.

25 Y. Zhang, L. Lin, J. Liu, J. Peng, Z. Chen and L. Chen, *Int. J. Hydrogen Energy*, 2021, **46**, 36629–36639.

26 V. Maheskumar, K. Saravanakumar, Y. Yea, Y. Yoon and C. M. Park, *Int. J. Hydrogen Energy*, 2023, **48**, 5080–5094.

27 J. Lin, H. Zhou, R. S. Amin, A. E. Fetohi, K. M. El-Khatib, C. Wang, L. Guo and Y. Wang, *Inorg. Chem. Front.*, 2023, **10**, 1294–1304.